Available online at www.sciencedirect.com

SCIENCE DIRECT®

Earth and Planetary Science Letters 228 (2004) 255–265

EPSL

www.elsevier.com/locate/epsl

Mantle deformation during slow seafloor spreading constrained by observations of seismic anisotropy in the western Atlantic

James B. Gaherty[a,*], Daniel Lizarralde[b], John A. Collins[c], Greg Hirth[c], Sangmyung Kim[b]

[a]*Lamont-Doherty Earth Observatory of Columbia University, 61 Rt 9W, Palisades, NY 10964, United States*
[b]*School of Earth and Atmospheric Sciences, Georgia Institute of Technology, United States*
[c]*Dept. of Marine Geology and Geophysics, Woods Hole Oceanographic Institution, United States*

Received 2 July 2004; received in revised form 8 October 2004; accepted 17 October 2004
Available online 21 November 2004
Editor: R.D. van der Hilst

Abstract

During mantle flow at mid-ocean ridges, viscous shear deformation imparts a structural fabric that remains in the lithosphere as it cools, preserving a record of ridge processes over time. This fabric can be detected by seismic imaging, as it produces an azimuthal anisotropy in the velocity of seismic waves that propagate in the shallow mantle. Using data from a novel seismic refraction survey in the western Atlantic, we found that the maximum *P*-wave velocity in the upper 10 km of mantle lithosphere formed at the slow-spreading Mid-Atlantic Ridge is parallel to the paleo-spreading direction, consistent with viscous shear deformation dominated by corner flow. The magnitude of the *P*-wave anisotropy is 3.4±0.3%, approximately one-half that found in lithosphere formed at faster spreading rates in the Pacific. Weaker anisotropy in the Atlantic suggests that more pervasive conductive cooling at slow spreading ridges increases the proportion of localized (brittle) deformation in the mantle lithosphere, thereby limiting the degree of viscous deformation. By scaling our field observations to laboratory experiments, we estimate that total viscous strain during slow seafloor spreading is of order 0.5, as opposed to ~1–2 for the fast-spreading case. Finally, our travel-time observations display an azimuthal asymmetry that can be interpreted in one of two ways: either the average elastic tensor in this region is not orthorhombic as is commonly assumed, or the underlying shear fabric is rotated ~15° relative to fossil spreading.

Keywords: seismic anisotropy; upper mantle; refraction; mantle flow

1. Introduction

Measurement of seismic anisotropy in oceanic lithosphere provides a direct means to study deformation associated with convection in the mantle. During

* Corresponding author. Tel.: +1 845 365 8450; fax: +1 845 365 8150.
E-mail address: gaherty@ldeo.columbia.edu (J.B. Gaherty).

0012-821X/$ - see front matter © 2004 Elsevier B.V. All rights reserved.
doi:10.1016/j.epsl.2004.10.026

seafloor spreading, peridotite mantle rock advects upward at the ridge and then outward with a velocity comparable to that of the separating plates. The viscous shear deformation associated with this advection is substantial. As the rocks cool to produce the oceanic lithosphere, they retain a record of this deformation in the form of coherent crystal-preferred orientation (CPO) of olivine grains (e.g., [1]). Under assumptions that appear to hold for the upper mantle, the orientation of the fabric is related to the mantle flow direction, and the fabric strength reflects the magnitude and coherence of viscous shear strain that the mantle has undergone [2–5]. Because olivine has highly anisotropic elastic properties, CPO direction and strength can be estimated from directional and/or polarization dependence of seismic wave speeds (e.g., [6]).

The relationship between spreading-derived olivine fabric and seismic anisotropy was originally proposed by Hess [7], based on the correspondence between the direction of fastest *P*-wave propagation and fracture zones in the Pacific. Analytical and numerical models of mantle flow and fabric development (e.g., [8–10]) suggest that lithospheric anisotropy is produced by simple-shear deformation beneath the ridge during corner flow, and that the direction of fast propagation corresponds to the spreading direction. While this model has proven successful in satisfying observations from the fast-spreading Pacific, it has not been extensively evaluated in other environments, including in lithosphere formed at slow spreading rates and at ridges strongly influenced by hotspots.

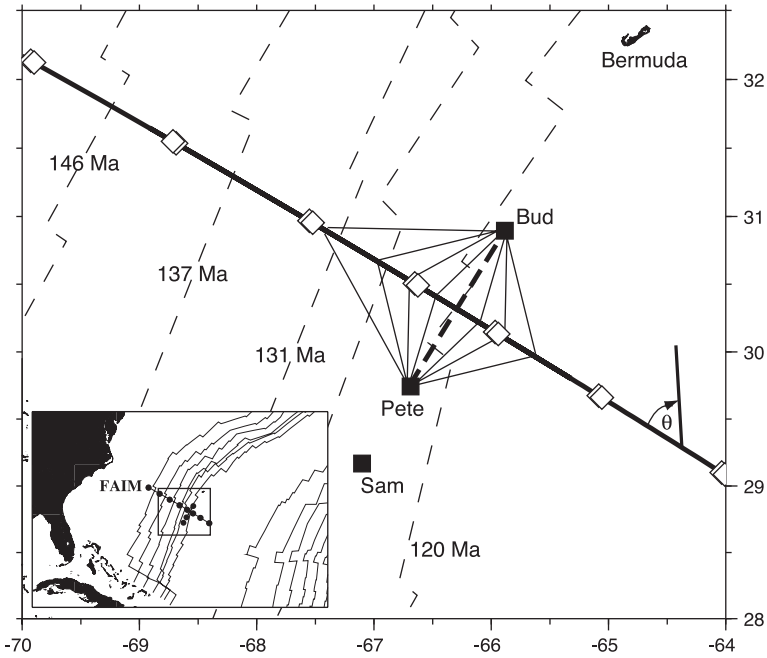

Fig. 1. Mercator projection of study region in the western Atlantic. Sixteen short-period, vertical-component OBS were deployed along a spreading-parallel transect in 3-km separated pairs spaced 80–120 km apart (open diamonds) and three OBS located ±75 and 150 km along a second line perpendicular to the first (solid squares). Thick solid line represents shot-line 1; airgun shots from this line recorded on the spreading-parallel transect were used to derive the line 1 model of Lizarralde et al. [11], while these shots recorded on the offline instruments Pete and Bud provide the azimuthal data modeled here (offline instrument Sam did not record line 1 shots with sufficient fidelity for analysis). Thin solid lines depict the source–receiver geometry of the azimuthal data at approximately 15° increments. Definition of relative azimuth θ used in the analysis is shown. Thick dashed line gives the geometry of shot-line 2; data recorded from these shots at Pete and Bud were used to derive the line 2 model of Lizarralde et al. [11]. Age contours are plotted in thin dashed line [12]. Inset shows western Atlantic location of the anisotropy experiment (box), including the complete set of ocean-bottom seismometers deployed in the experiment.

2. The FAIM seismic refraction experiment

In June 2001, we conducted the Far-offset Active-source Imaging of the Mantle (FAIM) seismic refraction experiment along an 800-km long transect in the western Atlantic (Fig. 1). A principal goal of this experiment was to quantify upper-mantle anisotropy in oceanic lithosphere formed at slow spreading rates. The experiment involved 16 short-period, vertical-component ocean-bottom seismometers (OBS) deployed both parallel and perpendicular to the inferred paleo-spreading direction. These instruments recorded shots from *R/V Maurice Ewing's* airgun array employing a slow shooting rate (4–7-min shot interval) designed to maximize the potential for recording *P* phases at large source–receiver offsets. Coherent *P*-wave arrivals were observed to 350-km distance, and the amplitude of this phase and its increasing and fast apparent velocity suggest that energy is propagating to ~25-km depth below the crust-mantle interface (Moho). Two-dimensional velocity models have been constructed for both the spreading-parallel and ridge-parallel lines, and these models and their interpretation in terms of lithospheric composition are presented elsewhere [11]. Here, we characterize the upper-mantle anisotropy beneath the eastern half of the array (Fig. 1), where seafloor magnetic anomalies indicate a history of very slow seafloor spreading (8–17 mm/year half rate) [12].

The 2-D models for lines 1 and 2 provide a minimum estimate of *P*-wave anisotropy. Both models are characterized by strong positive gradients with depth, with the spreading-parallel model approximately 2.5% faster throughout the upper 10 km of the mantle (Fig. 2). Higher *P*-wave velocities in the direction parallel to fossil spreading are consistent with anisotropy observations in the Pacific (e.g., [13]). However, velocities in two orthogonal directions cannot constrain the precise direction and magnitude of the anisotropy. To improve these constraints, we analyzed the travel times observed at the off-line instruments Pete and Bud from shots on line 1 (Fig. 3). These instruments recorded *P*-waves in a fan-shot mode with good signal to noise from shots at ranges of 75–250 km, with source–receiver azimuths relative to paleo-spreading spanning approximately 40–160° and 200–310°. Travel times of these arrivals were hand picked and corrected for variations in seafloor

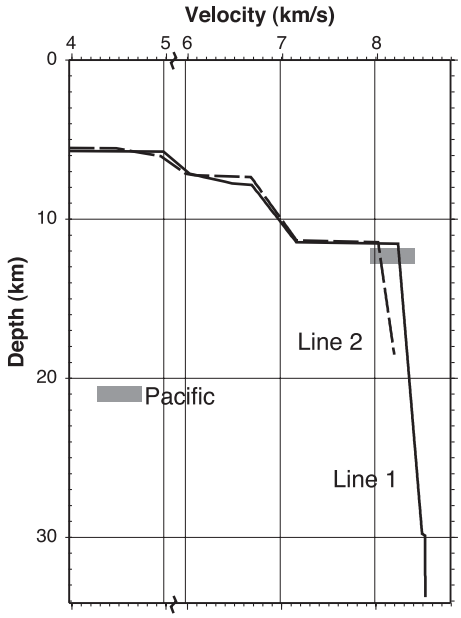

Fig. 2. Isotropic *P*-velocity models for line 1 (spreading-parallel) and line 2 (spreading perpendicular), from Lizarralde et al. [11]. *P*-wave velocity just below the Moho is 8.25 km/s on line 1 and 8.05 km/s on line 2. This corresponds to an apparent anisotropy of approximately 2.5%, which is roughly constant though the upper 10 km of the mantle. In a comparable experiment from the western Pacific [14,21], the spreading-parallel sub-Moho velocity is substantially higher (8.4 km/s), while the spreading-perpendicular velocity is lower (7.95 km/s) (grey bar). This implies that anisotropy in the Atlantic is smaller, or that the fabric is substantially rotated such that the fast and slow propagation directions do not correspond to spreading parallel and perpendicular orientations, respectively.

and basement depth and crustal thickness beneath the shots and receivers. The seafloor and basement corrections were derived from multi-channel seismic data along line 1 [11], and account for up to 0.3 s of the observed travel-time variability. The amplitude of this variability is of the same order as the mantle signal associated with anisotropy, but its spatial wavelength is much shorter, allowing us to correct for it without substantially biasing our result. Crustal thickness corrections are well constrained only near the receivers [11], but they are quite small, generally less than ±0.02 s. The corrected travel times characterize propagation through the mantle. To isolate the possible effect of anisotropy on these travel times, we calculated residuals relative to an isotropic model derived from the average of the lines 1 and 2 models of Lizarralde et al. [11]. Uppermost

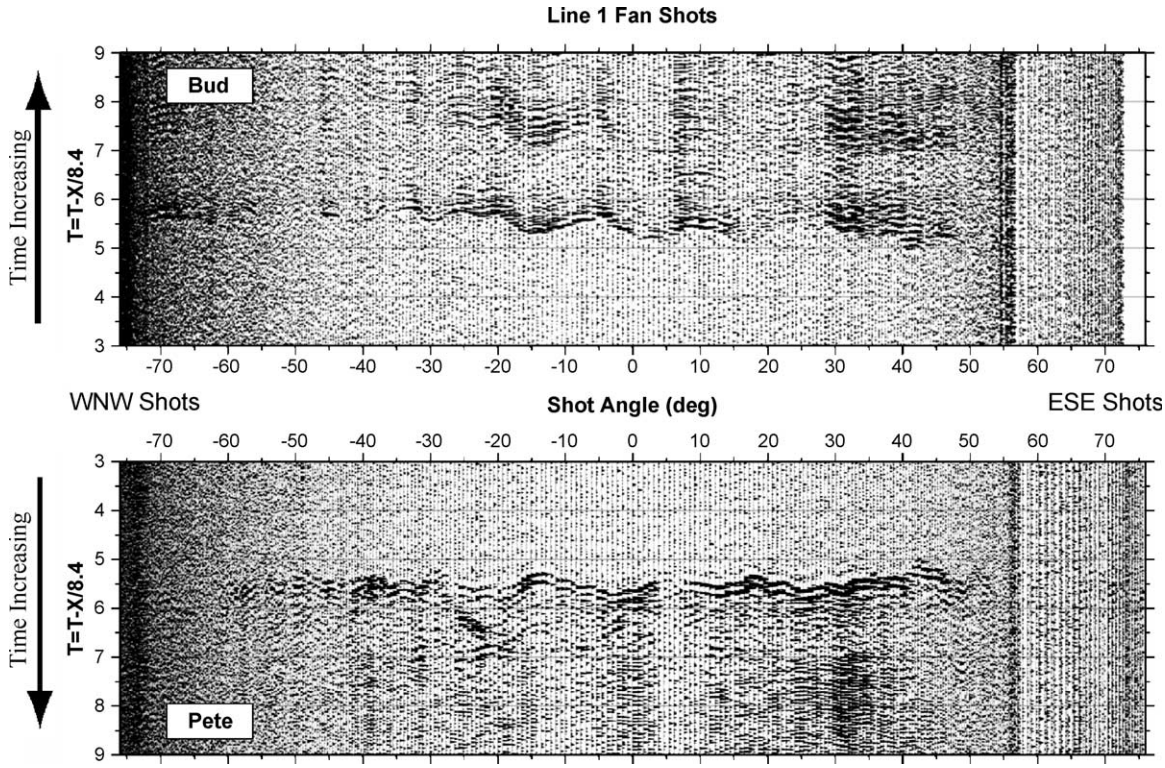

Fig. 3. Stacked seismograms of shots from line 1 recorded at offline instruments Pete and Bud, plotted as a function of shot angle. Shot angle is the angle between the receiver–source azimuth and line 2, and is measured at each receiver. Defined in this way, a single shot has a common shot angle at both Bud and Pete. Each stacked trace consists of five or seven individual seismograms. Source–receiver distance has a minimum value of 75 km at a shot angle of 0°.

mantle velocities are constrained to better than ±0.02 km/s in these models, and alternative isotropic reference models within this uncertainty range would have no discernable effect on our anisotropy estimates. Interpreting the resulting residuals in the context of azimuthal anisotropy requires that the observations have the same path length (e.g., [14]), so we normalize them to a common source–receiver offset of 75 km. This normalization is based on the assumption that the magnitude of the anisotropy does not vary in the upper ~10 km of the mantle; the nearly constant velocity difference between the lines 1 and 2 models (Fig. 2) suggests that this assumption is reasonable.

When plotted as a function of propagation azimuth (Fig. 4), these travel times display a strong long-wavelength variation, with slower (more positive) travel times arriving near a relative azimuth θ of 100–120° and 280–300°, nearly perpendicular to the fossil spreading direction. The residuals decrease strongly as the propagation azimuth approaches the fossil-spreading direction. To fill out the azimuthal sampling, we include a subset of the travel-time residuals observed from line 1 shots at line 1 stations at source–receiver azimuths of 0° and 180°. These data are restricted to sources and receivers within the region sampled by the fan-shot recordings (Fig. 1), and they are limited to observations at source–receiver offsets of 75–250 km so that all data have a consistent range of sampling depth. The reduced data in Fig. 4 exhibit substantial scatter, with short-wavelength variations most likely caused by unmodeled three-dimensional isotropic heterogeneity (including basement structure), as well as spatial variations in anisotropy. Basement structure may be particularly problematic, as it is very rough beneath the line 1 shots. While we correct the delay times for basement variations measured within the plane of line 1, these corrections

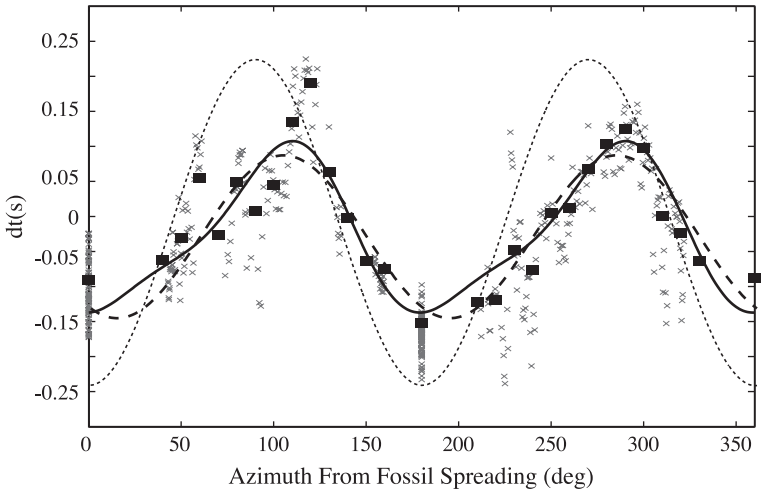

Fig. 4. Individual travel-time residuals (grey crosses) of line 1 shots recorded at offline stations Bud and Pete, along with times for several stations along line 1, plotted as a function of shot–receiver azimuth. Black squares represent weighted average of these data calculated in 20°-wide overlapping bins. Residuals are calculated relative to an isotropic velocity model, are corrected for variations in water depth, sediment thickness, basement topography and crustal thickness beneath each shot and receiver, and converted to a common offset of 75 km. Bud observations correspond to the source–receiver azimuths of 20–160°, Pete observations correspond to azimuths of 200–340°, and the line 1 stations provide observations at azimuths of 0° and 180°. Thick black lines display the predicted delay times for the best-fitting 2θ+4θ (solid) and 2θ (dashed) models described in text. For comparison, dotted line indicates the delay-time variation that would be expected for 2θ anisotropy with a magnitude of 6% oriented parallel to fossil spreading.

are approximate because most of the fan shots pierce the seafloor outside of this plane. The short-wavelength character of the remaining scatter is very similar to the variations observed in the basement corrections, suggesting that inaccuracy in this approximation is responsible for the scatter. To enhance the long-wavelength character of the azimuthal pattern, we calculated weighted averages of the residuals within overlapping azimuth bins (Fig. 3). The bins have a spacing of one-half the bin width, and linear weight function assigned to each datum ranges from one for a point in the center of the bin, to zero for a point at the bin edge. Bin width ranged from 4° to 20° azimuth.

3. Models of azimuthal anisotropy

We estimated the magnitude and direction of azimuthal anisotropy in the uppermost mantle using a least squares fit of the delay times by functions that are periodic in 2θ and 4θ, where θ represents source–receiver azimuth relative to fossil spreading [14–16]. If the anisotropy in the region is constant, then to first order the variation in travel time at a constant offset can be written as

$$\mathrm{d}t = a_0 + a_1\cos(2\theta) + a_2\sin(2\theta) + a_3\cos(4\theta) + a_4\sin(4\theta), \quad (1)$$

where a_0 is a static associated with unmodeled average isotropic velocity, and a_1, a_2, a_3 and a_4 are free parameters that are related to the strength and direction of azimuthal anisotropy [15]. In mantle rocks, the 4θ terms are predicted to be small, and many previous analyses of P-wave anisotropy have chosen to neglect it, i.e.

$$\mathrm{d}t = a_0 + a_1\cos(2\theta) + a_2\sin(2\theta) \quad (2)$$

(e.g., [14]). In either case, magnitude of the velocity anisotropy is calculated using the peak-to-peak difference in model delay times, which can be scaled to a velocity perturbation in percent,

$$\Delta V_\mathrm{p} = 200(V_\mathrm{max} - V_\mathrm{min})/(V_\mathrm{max} + V_\mathrm{min}) \quad (3)$$

where V_max and V_min represent the maximum and minimum P velocities in the medium, respectively. The orientations of these velocities (the so-called fast

and slow directions, θ_{fast} and θ_{slow}) correspond to the troughs and peaks of the travel-time vs. azimuth curve. In the 2θ+4θ models (Eq. (1)), θ_{fast} and θ_{slow} are independent of each other. In the 2θ models (Eq. (2)), θ_{fast} and θ_{slow} are orthogonal, and the anisotropy orientation and magnitude are trigonometric functions of a_1 and a_2.

We evaluated models that incorporated both the 2θ and 4θ terms, as well as those restricted to the 2θ terms. We applied these models to several data sets that differ in the choice for bin width in averaging the residuals, ranging from no binning to 20° (Table 1). For each model type and bin width, we provide the estimates of a_1 through a_4, as well as the inferred fast and slow directions and the magnitude of the anisotropy. The calculated model parameters are very stable with respect to choice of data averaging, and the range of derived anisotropy parameters provides a qualitative assessment of their uncertainty. Based on the 2θ+4θ models, P-wave anisotropy in this region has a fastest propagation direction at θ_{fast}=0±3° (i.e. spreading-parallel), a slowest propagation direction of θ_{slow}=112±3°, and a peak-to-peak dt variation of 0.26 s, which corresponds to P-wave anisotropy ΔV_p=3.4±0.3%. This model reduced the observed variance in the unbinned data by 69%. Nearly identical models were derived from independent fits to the Bud and Pete data, indicating that unmodeled lateral heterogeneity is not strongly biasing these estimates.

Most previous models of sub-Moho P-wave anisotropy restricted the parameterization to the dominant 2θ term. In our case, doing so resulted in a model with P-anisotropy of 3.0–3.1%, and a fast propagation direction of 14–18°, depending on choice of bin width (Table 1). The decreased fit of this model to the travel-time data is visually apparent (Fig. 4); in particular, it cannot match the skewness in the travel-time versus azimuth data, with the earliest arrivals roughly in line with fossil spreading, but the slowest arrivals rotated significantly (~20°) relative to the paleoridge. The 2θ model uses two fewer parameters, however, and the 4θ terms in the 2θ+4θ models have magnitudes that are comparable to their formal errors and are only 20–25% of the 2θ terms. F-test calculations suggest that from a statistical perspective the 2θ models are acceptable, and by Occum's razor, we would therefore prefer a 2θ model. There is a hidden complexity to this model, however, in that it ultimately requires a more complicated geodynamic interpretation. The 2θ+4θ models predict that the direction of fastest P-wave propagation is parallel to fossil spreading, consistent with fabric induced by two-dimensional corner flow oriented in the paleo-seafloor-spreading direction. In contrast, the 2θ model implies that the upper-mantle fabric is rotated 16±4° relative to fossil spreading, which suggests a three-dimensional subaxial flow field with a component in the ridge-parallel direction. The consistent pattern observed on Pete and Bud implies that this apparent flow-field rotation is present across the entire region, including across the intervening fracture zones. While it is enticing to interpret this anisotropy in terms of three-dimensional ridge dynamics, we feel that the two-dimensional

Table 1
Model parameters and associated anisotropy estimates

θ Model	Bin width (°)	$a_1\times10^{-1}$ (s)	$a_2\times10^{-1}$ (s)	$a_3\times10^{-1}$ (s)	$a_4\times10^{-1}$ (s)	θ_{fast} (°)	θ_{slow} (°)	ΔV_p (%)	VR (%)
4	–	−0.98±0.07	−0.42±0.10	−0.08±0.07	0.29±0.11	−2	110	3.2	69
2	–	−1.00±0.07	−0.54±0.08	–	–	14	104	3.1	67
4	4	−1.12±0.32	−0.56±0.18	−0.26±0.21	0.24±0.21	2	115	3.7	59
2	4	−0.92±0.24	−0.65±0.16	–	–	18	108	3.0	54
4	12	−1.07±0.32	−0.51±0.25	−0.17±0.26	0.20±0.28	3	112	3.4	67
2	12	−1.03±0.30	−0.57±0.24	–	–	15	105	3.1	64
4	20	−1.01±0.27	−0.49±0.23	−0.11±0.23	0.26±0.25	0	111	3.3	80
2	20	−1.03±0.28	−0.55±0.23	–	–	14	104	3.1	75

Model type of 4 corresponds to 2θ+4θ model, while 2 represents 2θ model. Bin width corresponds to width of overlapping triangular azimuthal bins used to average data; the models with no bin width are the fits to the raw unaveraged residuals. θ_{fast} and θ_{slow} are measured with respect to the paleo-spreading direction (line 1 azimuth). VR represents the reduction in variance associated with each model fit relative to the (averaged) data used for that model. Error bounds for model parameters correspond to the formal 95% confidence estimates.

ridge-perpendicular flow suggested by the $2\theta+4\theta$ model represents the simpler interpretation.

To our knowledge, this experiment represents the first unambiguous estimate of upper-mantle seismic anisotropy in slow-spreading oceanic lithosphere. An early refraction analysis in the slow-spreading Atlantic produced evidence of anisotropy but failed to robustly quantify it [17]. Surface-wave analyses from such regions do not distinguish shallow lithospheric structure from that of the deeper upper mantle [18,19]. Gaherty [20] documented lithospheric anisotropy adjacent to the slow-spreading Reykjanes Ridge, but the anomalous nature of that structure implies that it reflects the dynamics of hotspot-ridge interaction rather than slow seafloor spreading.

4. Discussion

At first glance, our results suggest that the spreading-derived model to explain *P*-wave anisotropy in the Pacific can be applied to the Atlantic. Shallow *P*-wave anisotropy has a fast azimuth that parallels the paleo-spreading direction, which is consistent with two-dimensional corner-flow models in which olivine fabric aligns with the flow direction [2,8,10]. Recent experiments on olivine aggregates have demonstrated that the fast seismic direction may be orthogonal to the flow direction if deformation takes place at high stress and/or water content [4], or under melt-rich conditions [5]. The strong correspondence between the fast propagation and fossil spreading directions in our data provides empirical evidence that these conditions were not prevalent during formation of the lithosphere in our study region.

With a magnitude of 3–4%, the *P*-wave anisotropy in this portion of the Atlantic is small compared to estimates of *P*-wave anisotropy from modern refraction data in fast-spreading regions. The most comparable result is from the Ngendei experiment in old Pacific lithosphere east of the Tonga trench, which had a similar spatial scale (offsets to 100–150 km) [14,21]. They found upper-mantle *P*-wave anisotropy of 5.5%, approximately 50% larger than that observed here. *P*-wave anisotropy of 6–7% was also found in two short-offset (<50 km) experiments on the fast-spreading East Pacific Rise [22,23]. Several older refraction experiments documented *P*-wave anisotropy ranging from 3% to 8% [13,16,17,24], but those experiments all predate the availability of repeatable airgun sources and high-quality ocean-bottom recordings, and they had poor control on overlying basement and crustal structure. Therefore, the relative accuracy of the older estimates is uncertain. Based on the more modern experiments, we conclude that the *P*-wave anisotropy produced during slow spreading (~10 mm/year half rate) in the Atlantic is approximately one-half the magnitude of that formed at faster spreading rates in the Pacific. This difference in the magnitude of anisotropy suggests that the processes responsible for the development and preservation of olivine CPO in the lithosphere depend on spreading rate.

There is strong evidence that the deformation styles active during seafloor spreading are dependent on spreading rate. In particular, localized (brittle) deformation is more prevalent near slow-spreading ridges. This is manifested in the greater abundance of large-displacement normal faults near slow-spreading ridges [25], an increase in the depth distribution of near-axis earthquakes [26], a greater proportion of extension accommodated through seismic slip [27], and localized shear fabric found in abyssal peridotites [28]. These observations presumably reflect the influence of conductive cooling (e.g., [29]), and they suggest that mantle flowing up and laterally outward in the upper 10 km beneath a slow-spreading ridge deforms at lower temperatures than at comparable depths beneath fast-spreading ridges. If this mantle upwelling is passive (driven by plate-separation forces located far from the ridge), then the total extensional strain associated with spreading should be largely independent of spreading rate. The abundant localized deformation at slow-spreading ridges therefore implies a correspondingly smaller proportion of distributed (viscous) strain within the uppermost mantle (e.g., [30]). Indeed, peridotite samples recovered from the Mid-Atlantic Ridge during Ocean Drilling Program Leg 209 appear to have undergone little bulk viscous deformation above a depth of 20 km [31]. We hypothesize that the strain localization responsible for ridge-parallel normal faulting persists to at least 10-km depth beneath the Moho (Fig. 5). Within this zone, bulk mantle rock is only weakly deformed, resulting in relatively small *P*-wave azimuthal anisotropy because

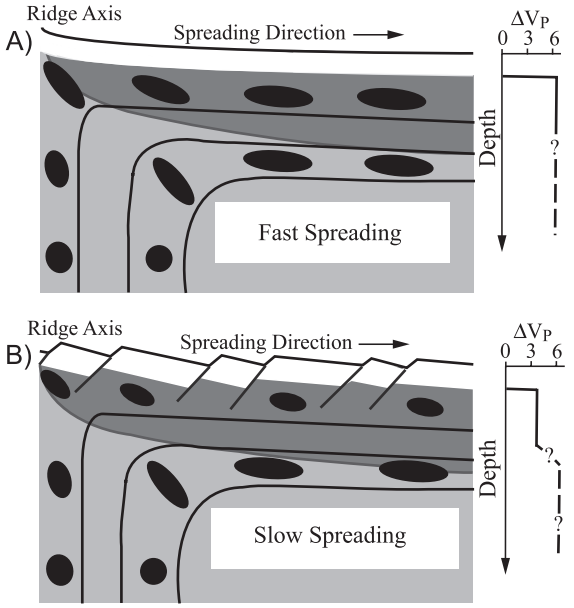

Fig. 5. Cartoon of mantle deformation and associated *P*-wave anisotropy profiles produced at end-member fast- and slow-spreading mid-ocean ridges. In each model, white layer depicts basaltic oceanic crust, dark grey represents the cooling lithosphere, and light grey corresponds to the underlying asthenosphere. Curves depict schematic flow lines for a passive model of seafloor spreading and black finite strain ellipses are shown. (A) Fast-spreading ridges are characterized by an axial high and minimal off-axis faulting. Underlying corner flow deformation occurs predominantly in the viscously deforming asthenosphere, resulting in large total strain with a horizontal orientation that produces azimuthal anisotropy of order 6%. Orientations of strain ellipses are based on numerical calculations of Blackman and Kendall [10]. (B) Slow-spreading ridges are characterized by an axial valley and pervasive off-axis faulting (black line segments). Conductive cooling produces a thickened lithosphere that impinges on corner flow, resulting in deformation that is partly accommodated by faulting to depths of up to 5–10 km beneath the Moho. As a result, the viscous strain the mantle at these depths is correspondingly reduced, as is the resulting anisotropy. In neither case is the anisotropy below ~10 km depth in the mantle (below Moho) well resolved. If our scenario is correct, then it suggests that anisotropy should increase with depth in slow spreading lithosphere. Diagrams are not to scale, but crustal thickness is approximately 5 km, and the thickness of the well-constrained anisotropic layer in the slow-spreading model is approximately 10 km.

the olivine fabric is poorly organized and not fully aligned within the horizontal (flow) plane [2].

If the olivine fabric is not fully aligned, the magnitude of *P*-wave anisotropy can be used to place bounds on the extent of intracrystalline viscous deformation. Olivine CPO (and thus seismic anisotropy) is strongly dependent on strain until it reaches a saturation point in the fabric strength. In olivine aggregates experimentally deformed in simple shear at a temperature of 1473 K, fabric evolved from weakly organized at shear strain $\gamma<0.5$, to very strong and parallel to the flow at $\gamma\sim4$–5 [3], while a similar experiment at slightly higher temperature (1573 K) produced strong, flow-parallel fabric at $\gamma\sim1.5$ [2]. The *P*-wave anisotropy in these experiments ranged from 3% for the weak-fabric case to ~15% for the strong fabric, the strength of which implies that the latter probably reached saturation [32]. It is difficult to directly relate the anisotropy derived from these synthetic olivine experiments to that observed in the field, which is expected to be smaller due to spatial averaging, non-optimal orientation of the olivine fabric relative to the propagation direction, and the presence of orthopyroxene and other minerals [33]. However, if we make the assumption that the Pacific *P*-wave anisotropy observations of 6–8% are at or beyond the saturation point (which is consistent with observations from ophiolites [33]), then the shear-strain implied by the observed 3–4% anisotropy is well below the saturation point, perhaps as low as $\gamma\sim0.4$–0.6. The additional strain needed to produce plate separation must occur via localized processes such as faulting.

Alternatively, it has been hypothesized that mantle upwelling beneath the slow-spreading ridges is partially driven by local buoyancy forces associated with melt and melt residuum, rather than solely by far-field tractions associated with plate motion (e.g., [34]). Numerical models of fabric development during buoyancy-enhanced spreading indicate that the resulting *P*-wave anisotropy within the shallow lithosphere is substantially smaller than that calculated for passive spreading models [10]. In the passive models, the anisotropy is quite strong because the fast (*a*) axes of olivine grains are efficiently aligned in a quasi-horizontal plane by the simple pattern of corner flow. In contrast, the buoyancy-enhanced models are characterized by a tight circulation pattern within the melting zone. This produces a fabric with olivine *a* axes that are less coherently aligned and less horizontal, and as a result, azimuthal anisotropy measured using horizontally propagating *P*-waves is not as strong. In this interpretation, the weak anisotropy does not imply weak shear deformation;

in the buoyancy-enhanced flow models, the shear strain beneath the Moho is quite high, but the predicted anisotropy does not closely correspond to the strain patterns because of the complexity of the flow [10]. Although our seismic data cannot distinguish between these two scenarios, we prefer the former because the recent peridotite observations showing minimal shear deformation [31] are not consistent with the large shear strains expected for buoyancy-driven flow.

A third, less likely, alternative is that the anisotropy is weaker under slow-spreading conditions because a substantial amount of deformation beneath the ridge was accommodated by diffusion (rather than dislocation) creep mechanisms. Coherent olivine CPO requires that creep occur in the dislocation regime. If slow spreading produces strain rates that are so low as to increase the proportion of diffusion creep, then a reduction in anisotropy is possible. This scenario requires that conditions in the melting region that control creep mechanism (in particular grain size and stress) are close to the point where diffusion and dislocation creep are equally likely. While these parameters are uncertain, extrapolation of laboratory data suggests that the upper 200 km of the mantle are well within the dislocation-creep regime [35,36].

Finally, it is possible that the Atlantic anisotropy is smaller because of a lower proportion of olivine in the lithospheric mantle (e.g., [31,37]). In fact, Lizarralde et al. [11] invoke a small amount of trapped gabbro to explain the sub-Moho velocity gradients on lines 1 and 2. However, assuming Voight averaging, the amount of gabbro required to fit the gradients (~15% by volume) is too small compared to that needed to produce the weak anisotropy (~50%).

The skewness observed in the travel times as a function of azimuth implies that the elastic tensor describing average *P*-wave propagation in this region does not exhibit purely orthorhombic symmetry (θ_{fast} and θ_{slow} are not orthogonal in our 2θ+4θ models) [15,38]. At the scale of individual rock specimens, the non-orthorhombic terms associated with the olivine fabric are generally quite small [32], and they are often neglected in seismic analyses [14,38]. These terms are somewhat greater if the averaging scale is increased to that of an ophiolite outcrop or larger [33]. Such asymmetry is often produced in numerical models of anisotropy if the finite strain of the rock varies spatially [39] or if the strain history is complex [40], suggesting that it should be expected in seismic travel-time data from many geologic settings. If our experience modeling such data is representative, it implies that the application of a 2θ model to data containing a subtle 4θ signal may result in a biased estimate of the apparent fast direction.

5. Conclusions

These results hold a number of implications for mid-ocean ridge dynamics. First, they support the notion that even at slow spreading rates, shallow melt-zone flow during seafloor spreading is predominantly two-dimensional, with the flow direction roughly parallel to the seafloor-spreading direction. They provide clear evidence that, at shallow depths (up to 10 km below the Moho), the horizontal olivine fabric produced during slow-seafloor spreading is substantially weaker than that produced during fast spreading. If this relatively weak fabric results from conductive cooling and strain localization, it implies that the amount of shear strain accommodated by intracrystalline viscous deformation in the bulk of the mantle away from localized shear zones is quite small, with extensional shear strains as low as 0.4–0.6. This quantification provides an important constraint on dynamic flow models of slow-seafloor spreading. Finally, our observations indicate that azimuthal estimates of seismic anisotropy contain a subtle 4θ signal which, if not modeled, may result in a rotation of the inferred fast propagation direction that could be misinterpreted in terms of a three-dimensional flow field.

Acknowledgments

We thank the crew of the R/V *Maurice Ewing*. D. Blackman and an anonymous referee provided helpful reviews. This research was supported by National Science Foundation grants OCE-0002417 and OCE-0002674. Lamont-Doherty Earth Observatory contribution 6689.

References

[1] A. Nicolas, N.I. Christensen, Formation of anisotropy in upper mantle peridotites: a review, in: K. Fuchs, C. Froidevaux (Eds.), Composition, Structure, and Dynamics of Lithosphere–Asthenosphere System, Geodyn. Ser., vol. 16, AGU, Washington, DC, 1987, pp. 111–123.

[2] S. Zhang, S.-I. Karato, Lattice preferred orientation of olivine in simple shear deformation and the flow geometry of the upper mantle of the Earth, Nature 389 (1995) 774–777.

[3] M. Bystricky, K. Kunze, L. Burlini, J.-P. Burg, High shear strain of olivine aggregates: rheological and seismic consequences, Science 290 (2000) 1564–1567.

[4] H. Jung, S.-I. Karato, Water-induced fabric transitions in olivine, Science 293 (2001) 1460–1463.

[5] B.K. Holtzmann, D.L. Kohlstedt, M.E. Zimmerman, F. Heidelbach, T. Hiraga, J. Hustoft, Melt migration and strain partitioning: implications for seismic anisotropy and mantle flow, Science 301 (2003) 1227–1230.

[6] M.K. Savage, Seismic anisotropy and mantle deformation: what have we learned from shear-wave splitting, Rev. Geophys. 37 (1999) 65–106.

[7] H. Hess, Seismic anisotropy of the uppermost mantle under oceans, Nature 203 (1964) 629.

[8] N.M. Ribe, Seismic anisotropy and mantle flow, J. Geophys. Res. 94 (1989) 4213–4223.

[9] D.K. Blackman, J.M. Kendall, P.R. Dawson, H.R. Wenk, D. Boyce, J. Phipps Morgan, Teleseismic imaging of subaxial flow at mid-ocean ridges: travel-time effects of anisotropic mineral texture in the mantle, Geophys. J. Int. 127 (1996) 415–426.

[10] D.K. Blackman, J.M. Kendall, Seismic anisotropy in the upper mantle: 2. Predictions for current plate boundary flow models, Geochem. Geophys. Geosyst. 3 (9) (2002) DOI:10.1029/2001GC000247.

[11] D. Lizarralde, J.B. Gaherty, G. Hirth, J.A. Collins, S. Kim, Spreading-rate dependence of melt extraction at mid-ocean ridges from mantle refraction data, Nature (2004) (in revision).

[12] R.D. Müller, W.R. Walter, J.-Y. Royer, L.M. Gahagan, J.G. Sclater, Digital isochrons of the world's ocean floor, J. Geophys. Res. 102 (1997) 3211–3214.

[13] G.B. Morris, R.W. Raitt, G.G. Shor, Velocity anisotropy and delay-time maps of the mantle near Hawaii, J. Geophys. Res. 74 (1969) 4300–4316.

[14] P.M. Shearer, J.A. Orcutt, Compressional and shear wave anisotropy in the oceanic lithosphere—the Ngendei seismic refraction experiment, Geophys. J. R. Astron. Soc. 87 (1986) 967–1003.

[15] G.E. Backus, Possible forms of seismic anisotropy of the uppermost mantle under oceans, J. Geophys. Res. 70 (1965) 3429–3439.

[16] R.W. Raitt, G.G. Shor, T.J. Francis, G.B. Morris, Anisotropy of the Pacific upper mantle, J. Geophys. Res. 74 (1969) 3095–3109.

[17] C.E. Keen, C. Tramontini, A seismic refraction survey on the Mid-Atlantic Ridge, Geophys. J. R. Astron. Soc. 20 (1969) 473–491.

[18] J.J. Lévêque, E. Debayle, V. Maupin, Anisotropy of the Indian ocean upper mantle from Rayleigh- and Love-waveform inversion, Geophys. J. Int. 133 (1998) 529.

[19] G. Silveira, E. Stutzmann, Anisotropic tomography of the Atlantic Ocean, Phys. Earth Planet. Inter. 4131 (2002) 1–12.

[20] J.B. Gaherty, Seismic evidence for hotspot-driven buoyant upwelling beneath the Reykjanes Ridge, Science 293 (2001) 1645–1647.

[21] P.M. Shearer, J.A. Orcutt, Anisotropy in the oceanic lithosphere—theory and observations from the Ngendei seismic refraction experiment in the south-west Pacific, Geophys. J. R. Astron. Soc. 80 (1985) 493–526.

[22] R.A. Dunn, D.R. Toomey, Seismological evidence for three-dimensional melt migration beneath the East Pacific Rise, Nature 388 (1997) 259–262.

[23] R.A. Dunn, D.R. Toomey, S.C. Solomon, Three-dimensional seismic structure and physical properties of the crust and shallow mantle beneath the East Pacific Rise at 9° 30′N, J. Geophys. Res. 105 (2000) 23537–23555.

[24] C.E. Keen, D.L. Barrett, A measurement of seismic anisotropy in the northeast Pacific, Can. J. Earth Sci. 8 (1971) 1056–1064.

[25] D.R. Bohnenstiehl, M.C. Kleinrock, Evidence for spreading-rate dependence in the displacement–length ratios of abyssal hill faults at mid-ocean ridges, Geology 28 (2000) 395–398.

[26] C.J. Wolfe, G.M. Purdy, D.R. Toomey, S.C. Solomon, Microearthquake characteristics and crustal velocity structure at 29°N of the Mid-Atlantic Ridge: the architecture of a slow-spreading segment, J. Geophys. Res. 100 (1995) 24449–24472.

[27] P.A. Cowie, C.H. Scholz, A. Malinverno, M.H. Edwards, Fault strain and seismic coupling on the East Pacific Rise, J. Geophys. Res. 98 (1993) 17911–17920.

[28] G.E. Jaroslow, G. Hirth, H.J.B. Dick, Abyssal peridotite mylonites: implications for grain-size sensitive flow and strain localization in the oceanic lithosphere, Tectonophysics 256 (1996) 17–37.

[29] N.H. Sleep, Formation of oceanic crust: some thermal constraints, J. Geophys. Res. 80 (1975) 4037–4042.

[30] M. Cannat, J.A. Karson, D.J. Miller, Proceedings of the Ocean Drilling Program, Initial Reports, vol. 153, Ocean Drilling Program, College Station, TX, 1995.

[31] P.B. Kelemen, E. Kikawa, D.J Miller, shipboard scientific party, Proceedings of the Ocean Drilling Program, Initial Reports, vol. 209, Ocean Drilling Program, College Station,TX, 2004, (in press).

[32] W. Ben Ismail, D. Mainprice, An olivine fabric database: an overview of upper mantle fabrics and seismic anisotropy, Tectonophysics 296 (1998) 145–157.

[33] N.I. Christensen, The magnitude, symmetry, and origin of upper mantle anisotropy based on fabric analyses of ultramafic tectonites, Geophys. J. R. Astron. Soc. 76 (1984) 89–111.

[34] E.M. Parmentier, J. Phipps Morgan, Spreading rate dependence of three-dimensional structure in oceanic spreading centers, Nature 348 (1990) 325–328.
[35] S.-I. Karato, P. Wu, Rheology of the upper mantle: a synthesis, Science 260 (1993) 771–778.
[36] G. Hirth, D. Kohlstedt, Rheology of the upper mantle and the mantle wedge: a view from the experimentalists, in: J. Eiler (Ed.), Inside the Subduction Factory, Geophys. Mono. Ser., vol. 138, AGU, Washington, DC, 2003, pp. 83–105.
[37] M. Cannat, Y. Lagabrielle, H. Bougault, J. Casey, N. de Coutures, L. Dmitriev, Y. Fouquet, Ultramfic and gabbroic exposures at the Mid-Atlantic Ridge: geological mapping in the 15N region, Tectonophysics 279 (1997) 193–213.
[38] S. Crampin, An introduction to wave propagation in anisotropic media, Geophys. J. R. Astron. Soc. 76 (1984) 17–28.
[39] D.K. Blackman, R. Wenk, J.M. Kendall, Seismic anisotropy in the upper mantle: factors that affect mineral texture and effective elastic properties, Geochem. Geophys. Geosyst. 3 (9) (2002) DOI:10.1029/2001GC000248.
[40] E. Kaminski, N.M. Ribe, Time scales for the evolution of seismic anisotropy in mantle flow, Geochem. Geophys. Geosyst. 3 (1) (2002) DOI:10.1029/2001GC000222.